Structural properties of molten dilute aluminium–transition metal alloys

2006 J. Phys.: Condens. Matter 18 6469

(http://iopscience.iop.org/0953-8984/18/28/003)

INSTITUTE OF PHYSICS PUBLISHING JOURNAL OF PHYSICS: CONDENSED MATTER

J. Phys.: Condens. Matter **18** (2006) 6469–6480 doi:10.1088/0953-8984/18/28/003

Structural properties of molten dilute aluminium–transition metal alloys

I Pozdnyakova[1], L Hennet[1], G Mathiak[2], J Brillo[2], D Zanghi[1], J-F Brun[1], S Brassamin[1], A Bytchkov[1], V Cristiglio[1], E Véron[1], G Matzen[1], G Geandier[3], D Thiaudière[4], S C Moss[5], F Spaepen[6], I Egry[2] and D L Price[1]

[1] Centre de Recherche sur les Matériaux à Haute Température, CNRS-CRMHT, 1d avenue de la Recherche Scientifique, 45071 Orléans cedex 2, France
[2] Institut für Raumsimulation, Deutsches Zentrum für Luft-und Raumfahrt e.V., Linder Höhe, 51147 Köln, Germany
[3] European Synchrotron Radiation Facility, BP 220, F-38043 Grenoble, Cedex, France
[4] Synchrotron Soleil, L'Orme des Merisiers, Saint-Aubin, BP 48, 91192 Gif-sur-Yvette, Cedex, France
[5] Department of Physics, University of Houston, Houston, TX 77204-5005, USA
[6] Division of Engineering and Applied Sciences, Harvard University, Cambridge, MA 02138, USA

E-mail: pozdnya@cnrs-orleans.fr

Received 16 March 2006, in final form 15 May 2006
Published 28 June 2006
Online at stacks.iop.org/JPhysCM/18/6469

Abstract

The short-range order in liquid binary Al-rich alloys (Al–Fe, Al–Ti) was studied by x-ray diffraction. The measurements were performed using a novel containerless technique which combines aerodynamic levitation with inductive heating. The average structure factors, $S(Q)$, have been determined for various temperatures and compositions in the stable liquid state. From $S(Q)$, the pair correlation functions, $g(r)$, have been calculated. The first interatomic distance is nearly temperature-independent, whereas the first-shell coordination number decreases with increasing temperature for all the alloys investigated. For the Al–Fe alloys, room-temperature scanning electron microscropy (SEM) studies show the formation of a microstructure, namely the existence of $Al_{13}Fe_4$ inclusions in the Al matrix.

1. Introduction

Transition metal aluminides are a technologically important class of alloys that combine high strength and resistance to environmental attack at elevated temperatures with low weight and low material cost. Recently, it was found that Al-based binary alloys with a few atomic per cent of iron and titanium exhibit superior mechanical properties [1]. The role of the additives in the

mechanical hardening is still unclear, but there is evidence of nanostructure formation in the solid phase Al–Fe alloys [2].

Phase diagrams of binary systems are often quite complex, displaying eutectics (signifying possible nanocluster formation) as well as intermetallic compositions. At the precise eutectic composition, the liquid phase transforms into two solid phases, while the opposite is true at intermetallic compositions. This indicates an interplay between energetic and entropic contributions to the thermodynamic potentials of the different phases. It also suggests the possibility of relatively stable clusters of intermetallic composition that persist into the liquid phase. The question then arises whether the structure of the liquid phase shows a distinct concentration dependence and, in particular, whether traces of intermetallic clusters exist in the liquid phase. In the case of dilute transition metal aluminides, there are suggestions of the formation of large Al clusters around the transition metal atom [3], which explains some of their interesting physical properties, in particular a remarkable increase in viscosity and a decrease in the coefficient of thermal expansion upon the addition of a few atomic per cent of the transition metals to pure molten aluminium [4].

A hybrid aerodynamic–electromagnetic levitation facility has recently been developed and successfully tested [5]. It combines the main advantages of the aerodynamic [6] and electromagnetic [7] levitation techniques, namely high sample stability, homogeneous melting, and good temperature control. With this new device, it was possible to study the local structure of Al-based liquid alloys, including compositions with rather low melting points, which would not have been accessible with standard electromagnetic levitation techniques.

In this paper, we report on x-ray diffraction measurements of molten dilute aluminium–transition metal alloys carried out on the ID15b beam line at the European Synchrotron Radiation Facility (ESRF) (Grenoble, France) using the aerodynamic–electromagnetic levitator for sample control and an image plate scanner for data acquisition. Diffraction patterns were taken for $Al_{95.8}Fe_{4.2}$, $Al_{92.5}Fe_{7.5}$, $Al_{99.5}Ti_{0.5}$ and $Al_{99}Ti_1$ over a wide temperature range in the liquid phase. In addition, the microstructures of the Al–Fe alloys were studied by SEM at room temperature.

2. Experimental details

2.1. Sample preparation

Samples of the investigated binary alloys were prepared at the Ames Laboratory of Iowa State University by melting together the required amounts of the constituent elements using an arc furnace with a water-cooled Cu crucible under an Ar atmosphere. From this, a rod of each composition was fashioned. In a second step, small pieces of the ingots were melted in a levitation process to obtain a homogeneous alloy and spherical shape. Samples weighing approximately 25–40 mg (2.7–3 mm diameter spheres) were prepared for the experiments.

2.2. SEM and EDX analysis

The samples were studied at room temperature by SEM using backscattered electron (BSE) imaging. The accelerating voltage used for these observations was 20 kV. As BSE production is directly proportional to the atomic number Z, the difference between Al and Ti or Fe was sufficiently large for an acceptable contrast. Thus it was possible to obtain pictures showing both microscopic composition variations and topographical information.

We also performed quantitative chemical analysis on various regions of the samples using energy dispersive x-ray (EDX) spectroscopy. Measurements were performed using two

accelerating voltages (10 and 20 kV) and the elemental compositions were obtained using the K and L spectral lines. To improve the accuracy of the analysis, we calibrated the instrument using a Co standard.

2.3. Heating system

For these experiments, we used a new aerodynamic–electromagnetic levitation chamber specially designed for the ID15b beamline at ESRF. Due to its compact design, this new hybrid heating system is particularly well suited for implementation at synchrotron or neutron beamlines. This device is described in detail in [5] and we give here only a short description of the working principles. The principal part is a Helmholtz-type coil producing a radio frequency (rf) magnetic field, and a BN conical nozzle that directed a gas jet supporting the sample. The levitator was housed in a stainless-steel cylinder of 320 mm in height and 200 mm in diameter, which was evacuated and subsequently filled with pure Ar.

A high-frequency generator with a maximum power of 5 kW and a frequency of 300 kHz was used for the power supply. The gas flow through the nozzle was adjusted using a PC-controlled mass flow controller that allowed a spherical sample to remain in a stable position without any contact with the nozzle. A video image of the sample was continuously displayed to monitor the sample during levitation and heating processes.

2.4. Temperature measurements

The temperature was measured with a single-colour infrared pyrometer, operating at $\lambda = 1.4\ \mu$m, aimed at the top of the sample. This method requires the knowledge of the spectral emissivity of the material to obtain the absolute temperature. For each sample, it was necessary to recalibrate the temperature with respect to a known melting or liquidus temperature. The absolute temperature T is obtained from the following approximation derived from Wien's law, which is accurate when the product λT is less than 3000 μm K:

$$\frac{1}{T} - \frac{1}{T_{\mathrm{pyro}}} = \frac{1}{T_{\mathrm{L}}} - \frac{1}{T_{\mathrm{L,pyro}}}. \tag{1}$$

Here, T_{pyro} is the output signal from the pyrometer, T_{L} is the liquidus temperature, and $T_{\mathrm{L,pyro}}$ is the pyrometer signal at this temperature. Equation (1) is valid only if the sample emissivity $\varepsilon(T)$ at the operating wavelength of the pyrometer remains constant over the experimental temperature range, which is a good approximation for most metals [8]. In order to check our calibration, we recorded temperatures during the free cooling of the sample after turning off the generator.

2.5. Diffraction measurements

A detailed description of the ID15b beam line can be found in [9]. For the experiments, we used a monochromatic beam of 88.54 keV ($\lambda = 0.14$ Å). The detection system was the MAR 345 online image plate scanner (2300 × 2300 pixels, with a pixel size of 0.15 μm). A 5 mm diameter cylindrical beam stop was placed in the direct beam. The distance between the sample and the image plate scanner was 400 mm, giving a usable Q-range of 0.8–14 Å^{-1}. The one-dimensional diffraction patterns were obtained by integrating the diffraction rings of the two-dimensional patterns using the MATLAB© and FIT2D software packages.

3. Results

3.1. Structure factors

The data analysis was based on the method of Wagner [10]. A correction for air scattering was made by subtracting an appropriate fraction of the scattered intensity measured using the empty levitator. The multiple scattering which contributes a few per cent to the diffracted beam was estimated using the procedure of Warren and Mozzi [11].

After these corrections, the x-ray intensity $I_s(Q)$ scattered by the sample is given by

$$\frac{I_s(Q)}{I_0(Q)} = A_{coh}(Q)I_{coh}(Q) + A_{incoh}(Q)I_{incoh}(Q) \tag{2}$$

where $I_0(Q)$ is the intensity of the incident beam measured with an ionization chamber, and A_{coh} and A_{incoh} are attenuation terms for the coherent and incoherent scattered intensities I_{coh} and I_{incoh}. The attenuation coefficients take into account the spherical shape of the sample and were determined using a numerical integration of the optical path of the x-ray beam over the irradiated volume. For this step, absorption coefficients were calculated from the x-ray cross sections compiled by McMaster *et al* [12]. Finally, the incoherent scattering intensity was calculated using the data of Balyusi [13].

According to the Faber–Ziman theory [14], the x-ray weighted average structure factor $S(Q)$ is related to the experimental coherent scattered intensity through the formula

$$S(Q) = \frac{I_{coh}(Q) - \langle |f(Q)|^2 \rangle}{|\langle f(Q) \rangle|^2} + 1 \tag{3}$$

where $\langle |f(Q)|^2 \rangle = c_{Al}|f_{Al}(Q)|^2 + (1 - c_{Al})|f_X(Q)|^2$ and $|\langle f(Q) \rangle|^2 = |c_{Al}f_{Al}(Q) + (1 - c_{Al})f_X(Q)|^2$

In equation (3), $|\langle f(Q) \rangle|^2$ and $\langle |f(Q)|^2 \rangle$ are, respectively, the square of the mean and the mean-square average scattering of the alloy, c_{Al}, is the atomic concentration of aluminium, and X = Fe or Ti. The atomic scattering factors were calculated from the values of Wassmaier and Kirfel [15] and the anomalous dispersion coefficients were taken from the Sasaki tables [16].

The structure factors for liquid $Al_{95.8}Fe_{4.2}$ and $Al_{99}Ti_1$, obtained at different temperatures in the stable liquid, are shown in figures 1 and 2, respectively. For the $Al_{95.8}Fe_{4.2}$ sample, the Bragg peaks appear on crossing the liquidus line at about 780 °C. The structure factors for the $Al_{92.5}Fe_{7.5}$ and $Al_{99.5}Ti_{0.5}$ alloys resemble those for $Al_{95.8}Fe_{4.2}$ and $Al_{99}Ti_1$. The structure of molten pure Al (99.999%) was measured for comparison, and the results are in agreement with previous studies [17]. The structural data for all compositions are compiled in table 1.

There are some common features for all compounds investigated. First, all experimental structure factors, $S(Q)$, exhibit two well-defined peaks at 2.64–2.8 and 4.8–5.1 $Å^{-1}$. Second, the first peak of the structure factors is symmetrical, except for the small deviations in $Al_{99.5}Ti_{0.5}$ alloy. Third, relatively far above the liquidus, at temperatures about 1000 °C, the ratio between the second and first peak positions, (Q_2/Q_1), is temperature-independent at values of about 1.8 for Al–Fe alloys and 1.86 for pure Al and Al–Ti alloys. The temperature dependence of the positions themselves seems to be different: for pure Al and Al–Ti alloys their values are temperature-independent, whereas for the Al–Fe alloys they increase slightly with temperature.

According to their phase diagrams, the Al–Fe alloys have higher liquidus temperatures than the Al–Ti alloys, where the liquidus temperatures are close to the melting temperature of Al. Therefore the former have a larger region of coexistence between liquid Al and intermetallics. Indeed, the crystallization of intermetallics was observed at about 779 °C in $Al_{95.8}Fe_{4.2}$, and at about 866 °C in $Al_{92.5}Fe_{7.5}$. We identified this phase as $Al_{13}Fe_4$ at both compositions. The room-temperature diffraction patterns for $Al_{95.8}Fe_{4.2}$ and $Al_{92.5}Fe_{7.5}$ after crystallization,

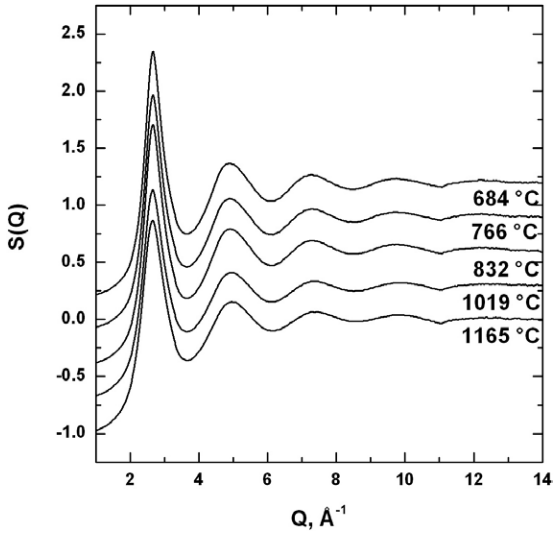

Figure 1. Average x-ray structure factor, $S(Q)$, for liquid $Al_{99}Ti_1$ at different temperatures. Spectra are shifted vertically for clarity.

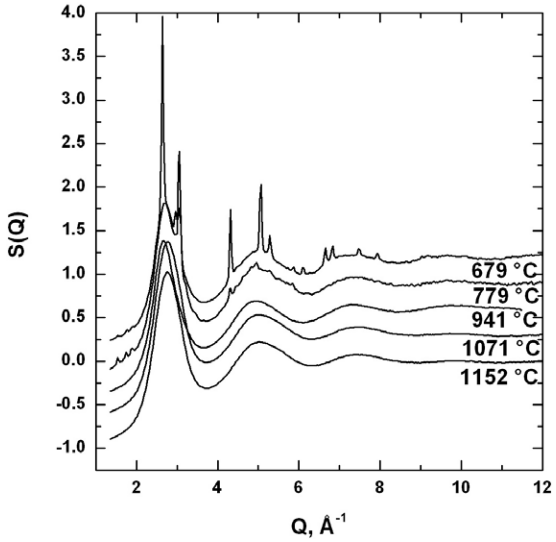

Figure 2. Average x-ray structure factor, $S(Q)$, for liquid $Al_{95.8}Fe_{4.2}$ at different temperatures. Spectra are shifted vertically for clarity. At 779 and 679 °C, the sample was partly solid.

together with reference patterns, are shown in figure 3. The pattern for $Al_{13}Fe_4$ was taken from JCPDF card #38-1147.

The speed of crystallization of the intermetallics depended on the cooling rate. The total structure factors for the $Al_{92.5}Fe_{7.5}$ alloy taken at different cooling rates are shown in figure 4. Apparently, the formation of the intermetallics is favoured during rapid cooling, and it might be possible to eliminate it using appropriate thermal conditions. To establish this, it is necessary to perform time-resolved x-ray diffraction measurements during cooling of the sample. On the other hand, the Al–Ti alloys appear homogeneous in the temperature range investigated,

Table 1. Summary of $S(Q)$ and g (r) data for metallic liquids studied in this work. The coordination numbers C_1 and C_1 (area) are determined as described in the text.

T (°C)	Q_1(Å^{-1})	Q_2 (Å^{-1})	r_1 (Å)	r_2 (Å)	C_1 (area)	C_1
			Al 99.999%			
738	2.64	4.89	2.82	5.25	11.6	8.715
800	2.64	4.89	2.8	5.25	11.2	8.245
999	2.64	4.92	2.8	5.25	11.1	8.105
			$Al_{95.8}Fe_{4.2}$			
679	2.64	5.07	2.82	5.02	11.347	9.418
779	2.73	4.95	2.76	4.99	11.017	9.1
941	2.67	4.965	2.8	5.21	11.689	8.892
1071	2.76	5.025	2.74	5.00	11.128	8.894
1152	2.76	5.025	2.74	5.01	10.905	8.234
			$Al_{92.5}Fe_{7.5}$			
698	2.685	4.95	2.78	5.09	11.984	8.955
754	2.73	4.805	2.78	4.9	11.879	9.464
866	2.73	4.95	2.76	4.96	11.072	8.976
916	2.76	4.92	2.74	4.91	11.175	8.812
1034	2.82	5.07	2.72	4.92	11.009	8.643
			$Al_{99}Ti_1$			
872	2.64	4.92	2.8	5.21	11.68	8.263
965	2.64	4.965	2.78	5.21	11.195	8.054
1058	2.64	5.01	2.78	5.21	11.113	8.114
1138	2.64	4.98	2.8	5.2	11.17	8.238
			$Al_{99}Ti_{0.5}$			
684	2.65	4.89	2.8	5.22	11.51	8.343
766	2.65	4.89	2.8	5.22	11.31	8.131
832	2.65	4.905	2.8	5.21	11.17	7.989
1019	2.66	4.935	2.78	5.18	10.998	7.509
1165	2.66	4.935	2.78	5.19	10.823	7.364

even though the phase diagram suggests intermetallic formation. To verify the absence of Al_3Ti intermetallics up to the crystallization temperature of aluminium, time-resolved x-ray experiments are also needed.

3.2. Pair-correlation functions

The x-ray weighted average pair correlation functions, $g(r)$, were obtained by a classical Fourier transform of $S(Q)$ using

$$g(r) - 1 = \frac{1}{2\pi^2\rho_0}\int_0^{Q_{\max}} Q(S(Q) - 1)\frac{\sin Qr}{r}M(Q)\mathrm{d}Q. \tag{4}$$

Here, $M(Q) = \sin(Q\pi/Q_{\max})/(Q\pi/Q_{\max})$ is the Lorch modification function used to force the end-points to go smoothly to zero. The average atomic number density, ρ_0, was calculated from the molar volume $\bar{v}$:

$$\rho_0 = \frac{N_A}{\bar{v}(T)} \tag{5}$$

where N_A is the Avogadro constant.

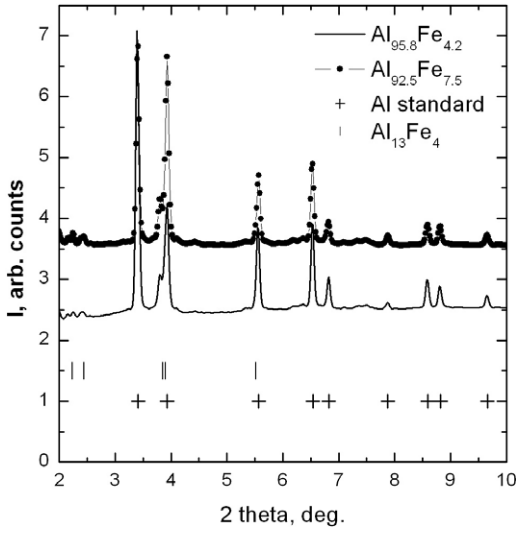

Figure 3. Room-temperature x-ray diffraction patterns for $Al_{95.8}Fe_{4.2}$ and $Al_{92.5}Fe_{7.5}$, together with reference patterns for Al and $Al_{13}Fe_4$.

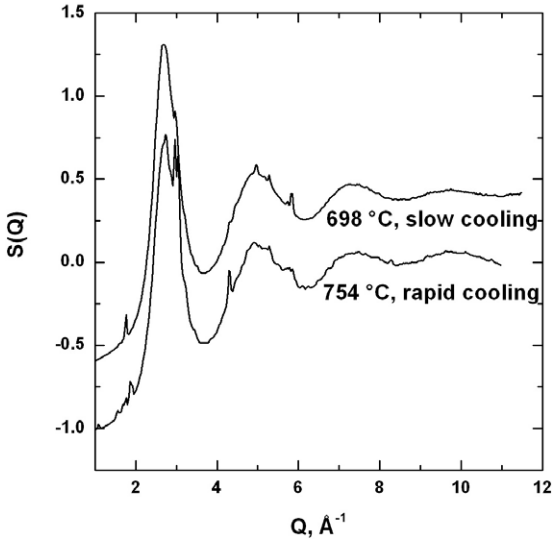

Figure 4. The dependence of the crystallization of intermetallic $Al_{13}Fe_4$ on the cooling rate in $Al_{92.5}Fe_{7.5}$ alloy.

The transition metal alloys in this study exhibit large negative deviations from volume additivity. Following Turnbull [3], the molar volume of a binary Al–X alloy is defined as

$$\bar{v} = c_{\mathrm{Al}}\bar{v}_{\mathrm{Al}} + (1 - c_{\mathrm{Al}})\bar{v}_{\mathrm{X}} \tag{6}$$

where $\bar{v}_{\mathrm{Al}}$ and $\bar{v}_{\mathrm{X}}$ are the partial molar volumes of Al and X (X = Fe or Ti). The values $\bar{v}_{\mathrm{Al}}$, $\bar{v}_{\mathrm{Ti}}$ and $\bar{v}_{\mathrm{Fe}}$ for dilute liquid alloys obtained at 900 °C are taken from [3]. The molar volume at other temperatures $\bar{v}(T)$ can be estimated by using the coefficient of volume thermal expansion of liquid Al, the majority component. The value determined from data given in [4] is $\alpha_{900} = 1.2 \times 10^{-4}\ \mathrm{K}^{-1}$. The temperature-dependent molar volume is:

$$\bar{v}(T) = \bar{v}(900\ ^{\circ}\mathrm{C})\,[1 + \alpha_{900}(T - 900)] \tag{7}$$

where temperatures are in °C. The density is obtained from:

$$\rho(T) = \frac{c_{\mathrm{Al}}A_{\mathrm{Al}} + (1 - c_{\mathrm{Al}})A_{\mathrm{X}}}{\bar{v}(T)} \tag{8}$$

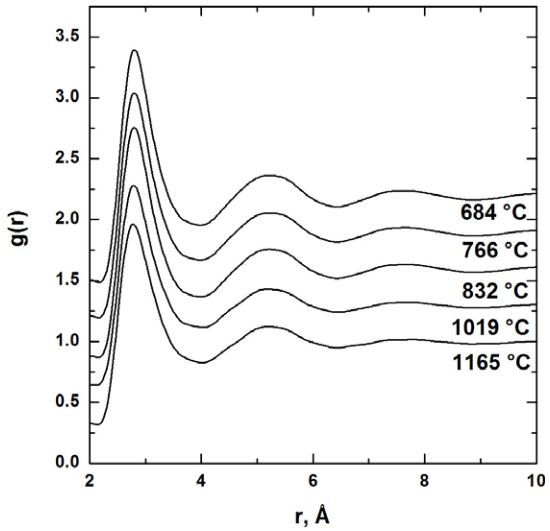

Figure 5. Average pair correlation function, $g(r)$, for liquid $Al_{99}Ti_1$ at different temperatures. The $g(r)$ curves are shifted vertically for clarity.

Table 2. Parameters used for the calculation of the number density for liquid dilute Al–Fe and Al–Ti alloys from [3].

Alloy	$\bar{v}_X$ (900 °C) ($cm^3\ mol^{-1}$)	$\bar{v}_{Al}$ (900 °C) ($cm^3\ mol^{-1}$)
Al–Ti	−45.6	11.7
Al–Fe	−9.3	11.7

where A_{Al} and A_X are the atomic weights of, respectively, Al and X. The parameters used for the density calculations are listed in table 2.

The pair correlation functions for the liquid $Al_{95.8}Fe_{4.2}$ and $Al_{99}Ti_1$ obtained at different temperatures in the stable liquid state are shown in figures 5 and 6, respectively. As shown on the figures, all curves are identical in shape, with the exception of the partly crystallized Al–Fe alloys, since the crystalline peaks were not removed from the raw data in order to see the complete picture.

There are two well-defined maxima at about 2.72–2.82 Å and 4.9–5.3 Å that correspond to the mean first and second interatomic distances in liquid alloys. The maximal contribution to the average pair correlation function, $g(r) = \sum W_{ij} g_{ij}(r)$, comes from the Al–Al pairs. The weighting factors W_{Al-Al} are 0.97, 0.98, 0.85 and 0.75 for $Al_{99}Ti_1$, $Al_{99}Ti_{0.5}$, $Al_{95.8}Fe_{4.2}$ and $Al_{92.5}Fe_{7.5}$, correspondingly. Coordination numbers are derived from $g(r)$ by two routines: first, by fitting the first peak of $T(r) = 4\pi\rho_0 r\ g(r)$ by a Gaussian and multiplying the area by the first mean interatomic distance r; second, by integrating over the whole area of $T(r)$ between the first and second minima. The method of calculation does not appear to affect the relative variations of the coordination numbers with temperature. The structural properties for all compositions are listed in table 1.

There is no temperature dependence of the first and second neighbour positions for pure Al and Al–Ti alloys. For the Al–Fe alloys, the position of the first peak in $g(r)$ seems to decrease slightly with increasing temperature. The coordination numbers decrease with increasing temperature for all alloys investigated.

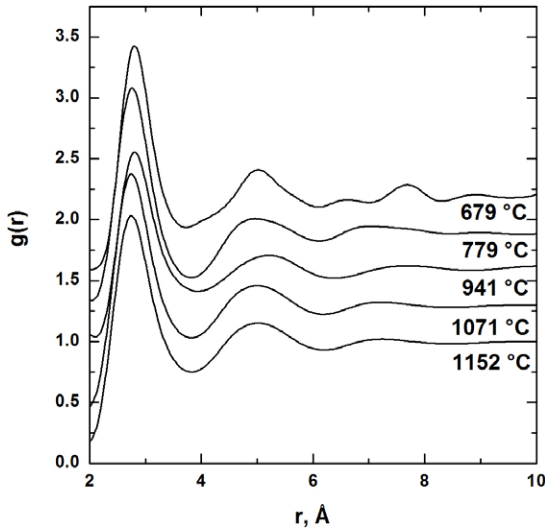

Figure 6. Average pair correlation function, $g(r)$, for liquid $Al_{95.8}Fe_{4.2}$ at different temperatures. The $g(r)$ curves are shifted vertically for clarity. At 779 and 679 °C, the sample was partly solid.

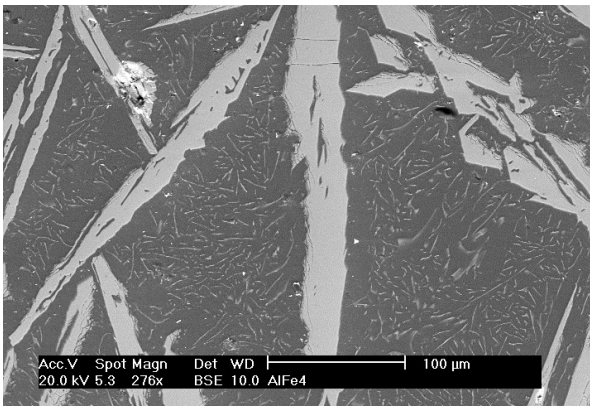

Figure 7. SEM image of the microstructure in $Al_{95.8}Fe_{4.2}$ alloy.

3.3. SEM imaging and EDX chemical analysis

Figures 7 and 8 present BSE images of $Al_{95.8}Fe_{4.2}$ alloys, showing the microstructures inside the sample. As BSE production varies proportionally with the atomic number, sections containing Fe appear brighter than those with Al. The pictures are similar for $Al_{92.5}Fe_{7.5}$ alloy.

The microstructure of Al–Fe alloys consists of needle-like iron aluminide intermetallic inclusions embedded in the Al matrix. There are two characteristic inclusion sizes: the bigger have a width of about 10–30 μm and length of about 100–400 μm; the smaller have a length of about 5–12 μm and a width of less than 1 μm. In $Al_{92.5}Fe_{7.5}$ alloy, the smaller inclusions form a net-like structure.

The EDX chemical analysis of the intermetallic inclusions gave an elemental proportion close to the composition $Al_{13}Fe_4$. This composition was confirmed by room-temperature x-ray diffraction, where no other intermetallic phase was found (figure 3). The matrix consists of pure

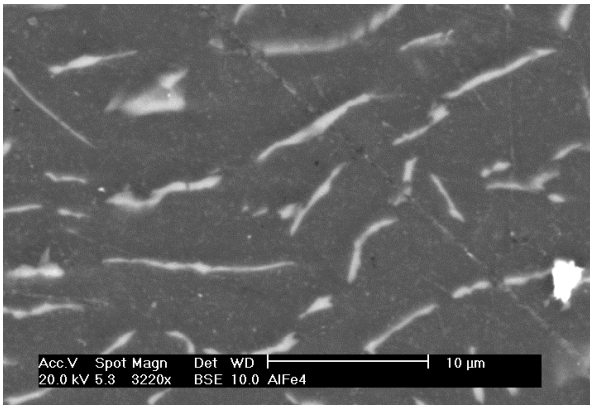

Figure 8. SEM image of the microstructure in $Al_{95.8}Fe_{4.2}$ alloy with higher magnification.

Table 3. The results of EDX chemical analysis for Al–Fe alloys.

Spectrum	O (at.%)	Al (at.%)	Fe (at%)	Total
		$Al_{95.8}Fe_{4.2}$		
Matrix	2.86	97.14		100
Inclusion		77.44	22.56	100
		$Al_{92.5}Fe_{7.5}$		
Matrix	2.77	97.23		100
Inclusion		77.35	22.65	100

aluminium. The results of the chemical analysis are summarized in table 3. It was impossible to identify the composition of the smaller intermetallic inclusions using K characteristic radiation, so the L-lines were used for that purpose.

4. Discussion

According to the criteria for a simple mixture approximated by the hard-sphere structure factor [18], namely the symmetry of the first peak in $S(Q)$ and the ratio of 1.86 between the position of the first two peaks Q_2/Q_1, which is nearly temperature-independent, liquid Al and Al–Ti alloys appear to be homogeneous liquids.

Al–Fe alloys also could be considered as homogeneous liquids, since the Fe solute shows solute–defect interactions that indicate a random distribution at high Al concentrations [19]. The second peak in $S(Q)$ does not show any peculiarities for all the alloys investigated, whereas a shoulder on the right side of the second peak is characteristic of icosahedral short-range order (SRO), for which evidence has been found in liquid Ni, Fe, Zr [20], as well as in $Al_{13}Fe_4$ and $Al_{74}Co_{26}$ [21] melts. This effect is found to be more pronounced when the melt is undercooled, so we would like to achieve the undercooled state of these alloys in future experiments.

The coordination numbers decrease with increasing temperature for all alloys studied, whereas the nearest-neighbour distances are nearly temperature-independent (table 1). This result is in accordance with numerous previous studies of liquid metals [17]. The decrease in the number of neighbouring atoms with increasing temperature is physically plausible, since it is necessary to accommodate the positive thermal expansion (and macroscopic density decrease) while the interatomic distances remain constant over a large temperature range.

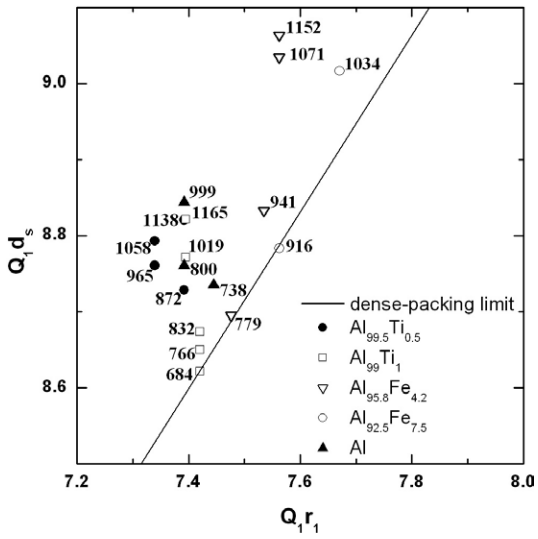

Figure 9. Scattering vectors of the first peaks in the structure factors $S(Q)$ of liquid alloys, scaled by the nearest-neighbour distance r_1 and the mean interatomic spacing d_s. The values near the data points indicate the temperature in °C.

For the Al–Fe alloys studied, the intermetallic inclusions disappear only at temperatures above 900 °C, and we thus cannot infer the temperature independence of the first interatomic distances due to the limited temperature range that is available. The values of coordination number are between 7.5 and 9.5 determined from the Gaussian fits, and between 11 and 12 determined by numerical integration. According to statistical physics considerations, the first coordination number in a simple liquid should be between 7 and 9 [22], as confirmed by the numerous molecular dynamic simulation studies for liquid metals [23].

By integrating the total area under the first peak of $g(r)$, one automatically includes the contributions from other neighbouring pairs, leading to the larger coordination numbers reported in the literature. However, independently of the way the coordination numbers were determined, the temperature and compositional trends were the same. The first-neighbour distances decrease with increasing Fe content in Al–Fe alloys, whereas no concentration dependence is observed for the coordination numbers.

From the available data, it is not possible to assign distances to specific pairs of atoms, since the Al–Al and Al–Fe (Al–Ti) distances differ by less than 1%. This would require independent measurements of the partial structure factors, by combining x-ray diffraction with neutron scattering and extended x-ray absorption fine structure.

It is useful to consider the classification of the structural properties of these liquid alloys according to the scheme proposed by Price and Moss [24]. In this scheme, the main peaks in $S(Q)$ are used to identify the type of ordering that may exist in the liquid or glass by scaling Q_1 with r_1, the first-nearest-neighbour distance, and d_s, the mean interatomic spacing ($\rho^{-1} = (\pi/6)d_S^3$). Values of Q_1 and r_1 have already been tabulated in table 1. Figure 9 gives the plot of $Q_1 r_1$ versus $Q_1 d_s$ for all the liquids studied here. The solid line drawn in the figure represents the limit for dense random packing of hard spheres, and it can readily be seen that all the liquids studied fall close to this line. Departures from the dense-packing limit became more pronounced with increasing temperature, as expected.

Previous x-ray diffraction studies for solid Al–Fe alloys with low Fe concentration (<5 at.%) did not show any diffraction peaks corresponding to Al–Fe intermetallic

compounds [1]. However, we see the formation of intermetallic $Al_{13}Fe_4$, at least at 4.22 at.% of Fe. Our results agree with recent studies where the first intermetallic compound formed in Al matrix was found to be $Al_{13}Fe_4$ [25]. Apparently, this phase cannot be suppressed by rapid quenching (figures 7, 8), in contradiction to earlier reports about the suppression of the $Al_{13}Fe_4$ phase [26]. According to the Al–Fe equilibrium phase diagram, while crossing the liquidus at an Fe concentration between 23.5 and 1 at.%, the crystallization of $Al_{13}Fe_4$ should happen. Our observation shows that this phase has much lower free energy, since no other phases were found even at extreme solidification conditions.

The microstructure formed in dilute Al–Fe alloys can play a crucial role in the high specific strength exhibited by these alloys. Intermetallic particles dispersed homogeneously through the Al matrix can enhance its strength by impeding dislocation motion [27].

Acknowledgments

We want to thank CNRS and DFG for financial support under the bilateral project 'Chemical ordering in high-temperature metallic melts'. Also, we would like to thank Dr Francis Millot for help with sample preparation, and the ID 15 beam line staff, in particular V Honkimäki and T Buslaps. S C Moss gratefully acknowledges the US Department of Energy for support via DE-FG02-04ER46160; his discussions with D Turnbull were most helpful.

References

[1] Sasaki H, Kita K, Nagahora J and Inoue A 2001 *Mater. Trans. JIM* **42** 1561
[2] Sakurai M, Matsuura M, Kita K, Sasaki H, Nagahora J, Kamiyama T and Matsubara E 2004 *Mater. Sci. Eng.* A **375–377** 1224
[3] Turnbull D 1990 *Acta Metall. Mater.* **38** 243
[4] Gebhardt E, Becker M and Dorner S 1953 *Z. Metalk.* **44** 573
[5] Mathiak G, Egry I, Hennet L, Thiaudière D, Pozdnyakova I and Price D 2005 *Int. J. Thermophys.* **26** 1151
[6] Landron C, Launay X, Rifflet J-C, Echegut P, Auger Y, Ruffier D, Coutures J-P, Lemonier M, Gailhanou M, Bessiere M, Bazin D and Dexpert H 1997 *Nucl. Instrum. Methods Phys. Res.* B **124** 627
[7] Herlach D, Cochrane R, Egry I, Fecht H and Greer A 1993 *Int. Mater. Rev.* **38** 273
[8] Krishnan S, Hansen G, Hauge R and Margrave J 1990 *High Temp. Sci.* **29** 17
[9] Tschentscher T and Suortti P 1998 *J. Synchrotron Radiat.* **5** 286
[10] Wagner C N J 1994 *J. Non-Cryst. Solids* **179** 84
[11] Warren B E and Mozzi R L 1966 *Acta Crystallogr.* **21** 459
[12] McMaster W H, Kerr Del Grande N, Mallett J H and Hubbell J H 1969 *Lawrence Livermore National Laboratory Report* UCRL-50174 Section II, Revision I
[13] Balyuzi H H M 1975 *Acta Crystallogr.* A **31** 600
[14] Faber T E and Ziman J M 1965 *Phil. Mag.* **11** 153
[15] Waasmaier D and Kirfel A 1995 *Acta Crystallogr.* A **51** 416
[16] Sasaki S 1989 *KEK Report* **88-14** 1
[17] Krishnan S and Price D L 2000 *J. Phys.: Condens. Matter* **12** R145
[18] Waseda Y 1980 *Structure of Non-Crystalline Materials* (New York: McGraw-Hill)
[19] Diak B J and Saimoto S 1997 *Mater. Sci. Eng.* A **234–236** 1019
[20] Schenk T, Holland-Moritz D, Simonet V, Bellissent R and Herlach D M 2002 *Phys. Rev. Lett.* **89** 075507
[21] Holland-Moritz D, Shenk T, Simonet V, Bellisent R, Convert P and Hansen T 2002 *J. Alloys Compounds* **342** 77
[22] Croxton C A 1980 *Statistical Mechanics of the Liquid Surface* (New York: Wiley)
[23] Ji M and Gong X G 2004 *J. Phys.: Condens. Matter* **16** 2507
[24] Price D L, Moss S C, Reijers R, Saboungi M-L and Susman S 1988 *J. Phys. C: Solid State Phys.* **21** L1069
Moss S C and Price D L 1985 *Physics of Disordered Materials* ed D Adler, H Fritzsche and S R Ovshinsky (New York: Plenum) pp 77–95
[25] Lee J-M, Kang S-B, Sato T, Tezuka H and Kamio A 2003 *Mater. Sci. Eng.* A **362** 257
[26] Thursfield G and Stowell M J 1974 *J. Mater. Sci.* **9** 1644
[27] Hauert R and Patscheider J 2000 *Adv. Eng. Mater.* **247** 2